JOURNAL OF GEOPHYSICAL RESEARCH, VOL. 102, NO. A12, PAGES 26,895-26,904, DECEMBER 1, 1997

Isotopic composition of solar wind neon measured by CELIAS/MTOF on board SOHO

R. Kallenbach,[1,10] F. M. Ipavich,[2] P. Bochsler,[1] S. Hefti,[1] D. Hovestadt,[3] H. Grünwaldt,[4] M. Hilchenbach,[4] W. I. Axford,[4] H. Balsiger,[1] A. Bürgi,[3] M. A. Coplan,[2] A. B. Galvin,[2] J. Geiss,[1,10] F. Gliem,[5] G. Gloeckler,[2] K. C. Hsieh,[6] B. Klecker,[3] M. A. Lee,[7] S. Livi,[4] G. G. Managadze,[8] E. Marsch,[4] E. Möbius,[7] M. Neugebauer,[9] K.-U. Reiche,[5] M. Scholer,[3] M. I. Verigin,[8] B. Wilken,[4] and P. Wurz[1]

Abstract. We present first results taken from the high-resolution mass time-of-flight spectrometer (MTOF) of the charge, element, and isotope analysis system (CELIAS) experiment on board the Solar and Heliospheric Observatory (SOHO) spacecraft launched in December 1995, concerning the abundance ratios of neon isotopes in the solar wind. We obtain the isotopic ratios $^{20}Ne/^{22}Ne = (13.8 \pm 0.7)$ and $^{20}Ne/^{21}Ne = (440 \pm 110)$, which agree with the values obtained from the Apollo foil solar wind experiments and which have been derived from measurements of solar particles implanted in lunar and meteoritic samples.

1. Introduction

Neon is the second most volatile element after helium. Its abundance in planetary materials (such as meteorites, terrestrial atmosphere, other planetary atmospheres, and lunar samples) is several orders of magnitude smaller than the solar abundance. The depletion in planetary matter is generally attributed to processes that took place in the early history of the solar system. First, the small natural neon abundance in planetary samples is due to the fact that at the ambient temperature and pressure in the presolar disk, interstellar dust and newly condensated samples were unable to incorporate large amounts of this noble gas. Second, neon that was originally trapped in solids was lost as a result of subsequent events. Such an event may have occurred, for instance, during the early evolution of Earth, when neon was degassed from the terrestrial interior into the atmosphere and then lost to space by hydrodynamical escape [*Hunten et al.*, 1991]. Quantitative loss of volatile components such as neon led to a substantial fractionation of the isotopic composition of the remaining fraction, in our case to the so-called planetary neon. Because of the general depletion of neon in planetary samples the only reliable inference for the isotopic composition of neon in the presolar nebula, and hence the local interstellar medium prior to formation of the solar system, can be drawn from the isotopic composition of solar neon. The isotopic composition of primordial neon has presumably been preserved in the solar interior because the Coulomb barrier of the neon isotopes is large enough to protect these nuclides from alteration by nuclear burning, even at the elevated temperatures prevailing in the solar center. Therefore it is safe to assume that solar neon composition has remained basically unchanged in space and time throughout the Sun and its history.

Determinations of the isotopic composition of neon in the solar wind are important because there is no better way to obtain information on the solar composition than through measuring longtime averages in the solar wind. *Bodmer and Bochsler* [1996] estimate the maximum isotope fractionation between solar surface neon and the interplanetary medium to be of the order of a few percent per mass unit. In view of the large differences among solar system materials, this estimation shows that neon in the solar wind has remained the most authentic sample for the isotopic composition of neon in the early solar nebula.

2. Instrumentation

The mass time-of-flight (MTOF) sensor (Figure 1) of the charge, element, and isotope analysis system (CE-

[1]Physikalisches Institut, University of Bern, Bern, Switzerland.
[2]Department of Physics and Astronomy, University of Maryland, College Park.
[3]Max-Planck-Institut für Extraterrestrische Physik, Garching, Germany.
[4]Max-Planck-Institut für Aeronomie, Katlenburg-Lindau, Germany.
[5]Institut für Datenverarbeitungsanlagen, Technische Universität, Braunschweig, Germany.
[6]Department of Physics, University of Arizona, Tucson.
[7]Institute for the Study of Earth, Oceans, and Space, University of New Hampshire, Durham.
[8]Institute for Space Physics, Moscow, Russia.
[9]Jet Propulsion Laboratory, Pasadena, California.
[10]Present address International Space Science Institute, Bern, Switzerland.

Paper number 97JA02325.
0148-0227/97/97JA-02325$09.00

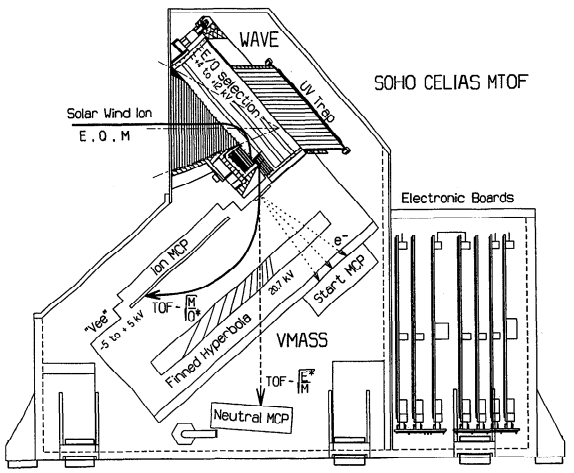

Figure 1. Schematic view of the SOHO/CELIAS/MTOF sensor.

LIAS) on board the Solar and Heliospheric Observatory (SOHO) spacecraft is an isochronous time-of-flight (TOF) mass spectrometer [*Hovestadt et al.*, 1995; *Hamilton et al.*, 1990] with a resolution $M/\Delta M$ of better than 100, which provides the possibility of resolving the different isotopes of almost all solar wind elements in the range from 3 to 60 amu. The instrument detects ions at solar wind bulk velocities of 300 to 1000 km/s corresponding to energies of about 0.3 to 3 keV/amu. The MTOF sensor was developed in the CELIAS consortium [*Hovestadt et al.*, 1995] under the lead of the University of Maryland (UMd) space physics group. The wide-angle variable energy (WAVE) entrance system was built under the guidance of the Physics Institute of the University of Bern (UoB) at INTEC, Bern. In collaboration with UMd, UoB contributed three-dimensional ion optical simulations and extensive calibrations of the integrated sensor. The Technical University of Braunschweig (TUB) contributed the data processing unit (DPU). Details on the principle of operation, the calibration of the instrument functions, the quantitative evaluation of TOF spectra, and the format of the data transferred by the telemetry can be found in the appendices.

3. Data Analysis

3.1. Fit of the Spectra

Figure 2 shows a spectrum where all pulse height analysis (PHA) words (see Appendix D2) of the first 200 days of 1996 have been collected. TOF channels have been put into bins of four, and the uncertainties of the data points have been estimated by the linear optimization algorithm of Rauch-Tung-Striebel [*Gelb et al.*, 1974], where the filter width corresponds to half the TOF resolution of the instrument, introducing a minor reduction of the peak resolution by 12%. This algorithm has been applied to improve the signal-to-noise ratio by a factor of 4 so that $^{21}Ne^+$ can be identified with high significance in the valley between the $^{20}Ne^+$ and $^{22}Ne^+$ peaks. $^{20}Ne^+$ and $^{22}Ne^+$ are clearly visible. The shoulder on the slope to the lower TOF channels of the $^{20}Ne^+$ peak has been identified as a systematic instrumental effect from electronic ringing. A shoulder of similar form, shift, and relative size can also be found at the left of $^{22}Ne^+$. In fact, all well-resolved peaks in the MTOF spectrum show this phenomenon at about 25 to 35 TOF channels at the left of the peak maximum. The shoulders cannot be attributed to the $^{40,42,44}Ca^{2+}$ interference because the observed shift in peak position of about 1.5% is 5 times larger than the upper limit expected from the simulations mentioned in Appendix C. Therefore all three peaks, $^{20}Ne^+$, $^{21}Ne^+$, and $^{22}Ne^+$, are described by the same model function [*Bochsler et al.*, 1997] with identical shape, including the shoulders, and identical width but with different amplitudes. The neon spectrum model function is given by the formula

$$
\begin{aligned}
F(t) = A_{20} \times \Big(\exp\Big[-\frac{(t-p_{20})^2}{2s^2}\Big] + \frac{b}{1+\frac{(t-p_{20}+l)^2}{w^2}} \\
+ c \times \exp\Big[-\frac{(t-p_{20}+r)^2}{2u^2}\Big]\Big) \\
+ A_{21} \times \Big(\exp\Big[-\frac{(t-p_{21})^2}{2s^2}\Big] + \frac{b}{1+\frac{(t-p_{21}+l)^2}{w^2}} \\
+ c \times \exp\Big[-\frac{(t-p_{21}+r)^2}{2u^2}\Big]\Big) \\
+ A_{22} \times \Big(\exp\Big[-\frac{(t-p_{22})^2}{2s^2}\Big] + \frac{b}{1+\frac{(t-p_{22}+l)^2}{w^2}} \\
+ c \times \exp\Big[-\frac{(t-p_{22}+r)^2}{2u^2}\Big]\Big) \quad (1)
\end{aligned}
$$

with t being the TOF channel number and with the following free fit parameters: $A_{20,21,22}$ are the amplitudes of the $^{20,21,22}Ne^+$ peaks, p_{20} is the main Gaussian peak position of $^{20}Ne^+$, l is the shift of the Lorentzians against the main Gaussians for all three peaks of $^{20,21,22}Ne^+$, r is the shift of the ringing peaks against the main Gaussians, b is the relative amplitude of the Lorentzians compared to the main Gaussians, c is the relative amplitude for the ringing peaks, s is the width of the main Gaussian peaks, w is the width of the Lorentzian peaks, and u is the width of the ringing peaks. The Gaussian peak positions $p_{21,22}$ of $^{21,22}Ne^+$ are kept fixed at their calibrated TOF channels. The total amplitudes $A_{20,21,22}$, the widths w and u, and the relative amplitudes b and c give the quantities for $^{20,21,22}Ne^+$, which then have to be corrected for the $^{40,42,44}Ca^{2+}$ interferences that are estimated from the $^{40}Ca^+$ counts in the same spectra, using the model of the instrument fractionation and assuming terrestrial isotopic abundance ratios for the calcium isotopes [*Anders and Grevesse*, 1989]. More precise values can be given once the CELIAS/MTOF calcium isotope measurements are evaluated thoroughly.

As can be calculated from Table 1, the integrated counts for $^{20,21,22}Ne^+$ are 83683 ± 396, 189 ± 48, and 6433 ± 89. This calculation gives the count ratios

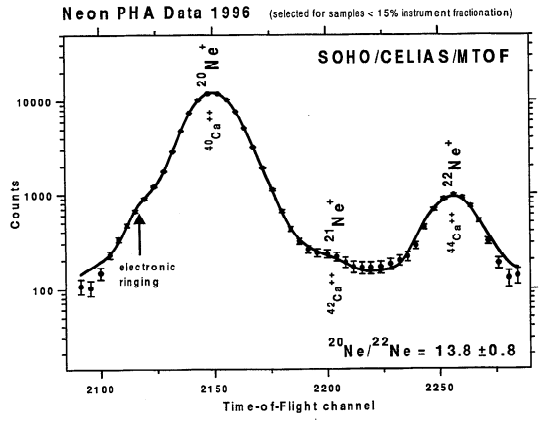

Figure 2. Time-of-flight spectrum derived from the PHA words of the first 200 days of 1996 filtered with respect to instrument fractionation with a window of ±15%. TOF channels have been put into bins of four, and the uncertainties of the data points are estimated with the linear optimization algorithm of Rauch-Tung-Striebel [*Gelb et al.*, 1974]. The filter width in the algorithm is kept at half the TOF resolution of the instrument, introducing only a minor reduction of the peak resolution by 12%. However, the algorithm improves the precision of the abundance measurement of $^{21}Ne^+$ drastically from about 100% uncertainty to 25%. A background of 2600 counts has been subtracted in the diagram but has been included in the error estimation. The arrow marks an electronic ringing effect that is observable at about 25 to 35 channels at the left of any well resolved time-of-flight peak. The interference of the doubly charged calcium isotopes cannot be resolved by the instrument but has to be corrected from the neon counts by using a model calculation of the instrument response and the actually detected singly charged calcium counts. The solid line represents the fitted model function of the TOF response.

$^{20}Ne^+/^{22}Ne^+ = (13.0 \pm 0.2)$ and $^{20}Ne^+/^{21}Ne^+ = (440 \pm 110)$. Figure 3 shows a magnification of the $^{21}Ne^+$ region where the uncertainty is illustrated by plotting the model function for the best and two extreme amplitudes A_{21}. The errors given here are only statistical and are dominant for the ratio $^{20}Ne^+/^{21}Ne^+$. To obtain the isotope abundance ratio for $^{20}Ne^+/^{22}Ne^+$ and its uncertainty, however, the count ratios have to be corrected by the efficiency ratios derived from the calibrated instrument functions with their uncertainties. This process is discussed by a further evaluation of the TOF spectra in the following subsection.

3.2. Estimate of the Experimental Uncertainty

Grouping the neon data into thirty 1%-wide classes of instrument fractionation (Figure 4) in the range where the efficiency ratio for the two isotopes varies between 0.85 and 1.15 leads to the conclusion that the unity fractionation has been found with an error of 2.7%, which can be considered as a systematic offset of the instrument fractionation scale. In the range where the efficiency ratio varies between 0.95 and 1.05 the statistical error and the estimated variation of the corrected abundance ratios in the individual 1% classes by the uncertainty of the instrument functions (assuming the offset of unity fractionation is known exactly) are approximately equal (2.6% and 2.8%). An analysis of this range gives an abundance ratio $^{20}Ne/^{22}Ne = (13.8 \pm 0.5)$. However, the systematic offset of 2.7% in finding the unity fractionation in parameter space has to be included in the total uncertainty until further evaluations of MTOF data have been performed. Therefore 2.6% is the statistical uncertainty, 2.8% is the uncertainty originating from the calibrated instrument functions, and 2.7% is taken as uncorrected systematic offset, adding quadratically to 4.7%. This finally results in $^{20}Ne/^{22}Ne = (13.8 \pm 0.7)$.

4. Results

Taking the analysis of PHA data and TOF spectra, we conclude that the isotopic abundance ratios of solar wind neon are $^{20}Ne/^{22}Ne = (13.8 \pm 0.7)$ and $^{20}Ne/^{21}Ne = (440 \pm 110)$. Both ratios agree with ratios determined by other methods, such as the Apollo foil experiments and solar particle composition analysis from lunar samples [*Geiss et al.*, 1972; *Benkert et al.*, 1993]. CELIAS/MTOF has such good counting statistics that

Table 1. Fitted Parameters of the Model Function for the Neon PHA Spectrum

	$A_{20,21,22}$	$p_{20,21,22}$	$^{20,21,22}Ne^+$ Counts	$^{40,42,44}Ca^{2+}$ Counts	$Ca^{2+}/(Ne^+ + Ca^{2+})$
$^{20}Ne^+$	8233 ± 30	2150.8	83683 ± 396	6829 ± 220	7.5 %
$^{21}Ne^+$	21.4 ± 4.3	2204.4	189 ± 48	46 ± 7	19.6 %
$^{22}Ne^+$	599 ± 8	2256.8	6433 ± 89	147 ± 12	2.2 %

The first column shows the fitted peak amplitudes $A_{20,21,22}$ and their 1σ errors determined with the method of maximum likelihood, the second column shows the fitted peak position p_{20} and the fixed calibrated peak positions $p_{21,22}$, the third column shows the total number of neon counts $^{20,21,22}Ne^+$ already corrected for the doubly charged calcium interference $^{40,42,44}Ca^{2+}$ of the fourth column, which is also given as a percentual number in the fifth column. The parameters that are equal for all three isotopes have been fitted as $s = 10.66$, $b = 0.495$, $l = 1.71$, $w = 10.78$, $c = 0.035$, $r = 31.66$, and $u = 5.71$.

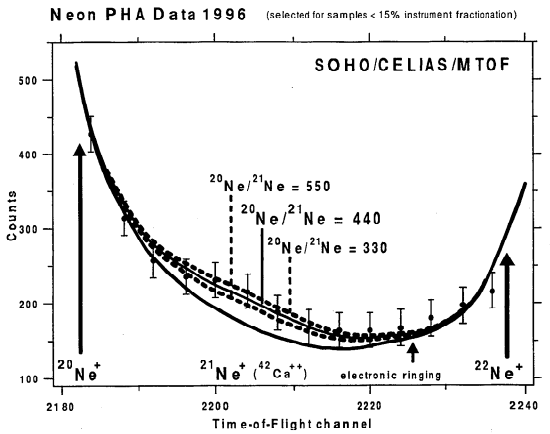

Figure 3. A magnification of the $^{21}Ne^+$ region between the signatures of $^{20}Ne^+$ and $^{22}Ne^+$. The bottom solid line represents the fitted model function without the $^{21}Ne^+$ peak, and the top solid line represents the best fit including $^{21}Ne^+$. In the model function the electronic ringing peak of $^{22}Ne^+$ is visible. The dashed lines reflect the cases with the $^{21}Ne^+$ amplitudes 25% larger or smaller. These correspond to the variance limits of maximum likelihood. A background of 2600 counts has been subtracted in the diagram but has been included in the error estimation.

a variation of the abundance ratios with solar wind parameters might become observable. Figure 5 shows the result of a preliminary analysis of the variation of $^{20}Ne/^{22}Ne$ with the solar wind bulk velocity. Although at first glance a trend can be seen in the sense that the ratio is lower for higher speeds, one needs to be careful not to be misled by effects of the instrument fractionation. Also, the observed values are still statistically compatible with an isotopic abundance ratio that is independent of solar wind velocity. However, future analysis with an extended data set may provide sufficient statistical accuracy to test the model of *Bodmer and Bochsler* [1996], which predicts a weak isotope fractionation in the inner corona by variable Coulomb drag.

5. Discussion

Table 2 lists isotopic ratios as determined in different solar system materials, the best estimate of the local interstellar medium as derived from the anomalous cosmic ray component, and the galactic cosmic rays. Our new solar wind values confirm the determinations obtained with the Apollo Solar Wind Composition experiment [*Geiss et al.*, 1972]. Pending a further evaluation of a more extensive time series to be obtained with CELIAS/MTOF, we believe that our solar wind values must be within a few percent of the true solar composition values. Clearly, the planetary types of neon differ significantly from the solar value. Although there is no room for a detailed discussion, we also emphasize the wide spread of isotopic $^{20}Ne/^{22}Ne$ ratios among different populations of solar energetic particles. The $^{20}Ne/^{22}Ne$ ratios measured in the flare events of October 30 and November 2, 1992 [*Selesnick et al.*, 1993], have been slightly corrected for a Q/M fractionation process known from gradual flares and agree with the solar wind value. Significant deviations were observed for other flares, especially ^{3}He-rich flares, and for the longtime averages derived from lunar samples [*Benkert et al.*, 1993]. In fact, it is not surprising to find such large variations in view of the selectivity of the flare acccleration processes involved. In contrast to the solar wind population, which represents the vast majority of solar particles in the interplanetary medium, solar energetic particles represent only a minor fraction of a population that has undergone a complicated sequence of processes. The recently found strong enrichment of ^{22}Ne in ^{3}He-rich flare particles [*Mason et al.*, 1994] is a striking feature of these processes. It has in fact been

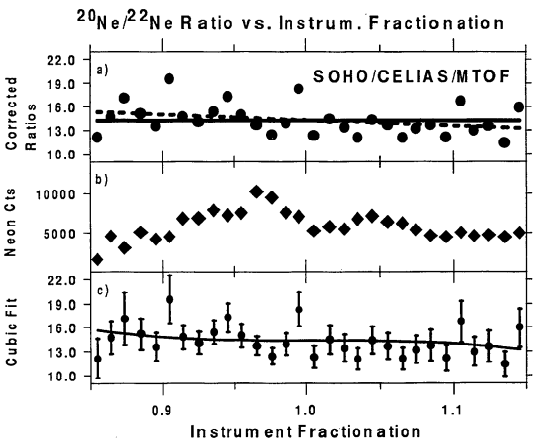

Figure 4. (a) Demonstration that the abundance ratio $^{20}Ne/^{22}Ne$ of the flight data, which is corrected for the instrument fractionation and for the doubly charged calcium interference, is almost independent on the instrument fractionation. A least squares fit to the slope suggests that the instrument fractionation is underestimated by about 25%, corresponding to the absolute calibration error of 25% in the instrument functions discussed in Appendix B. (b) Total number of neon counts in fractionation windows of 1% width versus instrument fractionation. More particles are collected in the vicinity of unity fractionation than away from unity. This finding is reasonable because fewer counts have to be expected on the slopes of the instrument response functions than at the plateau around maximum sensitivity. (c) For a more detailed analysis the statistical uncertainty from the total number of neon counts in each fractionation window of Figure 4b, the respective background counts, and the uncertainty of the calibration are taken into account, giving ratios with error bars. A χ^2 fit provides a cubic polynomial that is practically flat in the range 1.00 ± 0.05. In this range a value $^{20}Ne/^{22}Ne = (13.8 \pm 0.5)$ is obtained by adding all counts corrected for the instrument fractionation. However, the cubic fit suggests that the unity fractionation only has been found with an error of 2.7%, which can be considered as a systematic offset of the instrument fractionation scale.

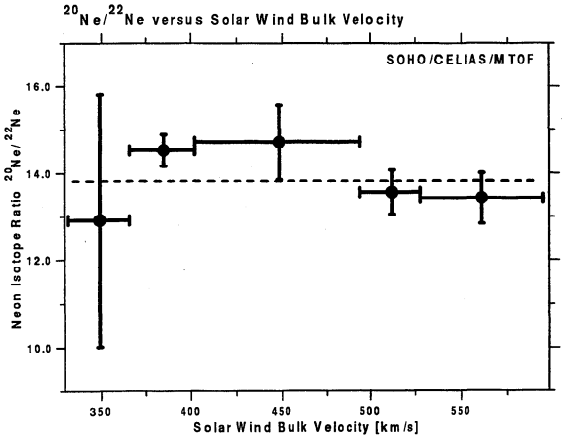

Figure 5. $^{20}Ne/^{22}Ne$ versus solar wind bulk velocity. The vertical error bars represent the uncertainty due to counting statistics, whereas the horizontal bars visualize the range of the solar wind bulk velocity for each measurement.

predicted [*Bochsler and Kallenbach*, 1994; *Kallenbach*, 1994], and similar enrichments with relevance for cosmochemical processes have to be expected for other isotopes. The presently achieved precision for the determination of ^{21}Ne abundance is not yet sufficient to be used for geochemical comparisons, for example, of terrestrial neon with solar neon. However, analysis of longer time series should allow such investigations. The most important goal, however, remains the comparison of the $^{20}Ne/^{22}Ne$ ratio in different solar wind regimes, which will make it possible to assess the authenticity of solar wind samples with respect to the source composition, i.e., with the $^{20}Ne/^{22}Ne$ ratio in the outer convective zone of the Sun.

6. Conclusion

One of the aims of the SOHO space mission is to provide correlated measurements of optical and particle instruments. The fact that the SOHO/CELIAS/MTOF in situ measurement of the solar wind neon isotopic composition reproduces very well the results obtained from returned lunar and meteoritic samples and from the Apollo foils encourages further studies of the solar wind isotopic composition in different solar wind regimes. The present analysis shows that the CELIAS/MTOF instrument can supply time-resolved data that can be correlated with the solar wind bulk velocity, kinetic temperature, and density measured by the CELIAS proton monitor (F. M. Ipavich et al., The solar wind proton monitor on the SOHO spacecraft, submitted to *Journal of Geophysical Research*, 1997, hereinafter submitted manuscript). In the same way, correlations with the optical observations from other SOHO instruments should be feasible.

Appendix A: Principle of the MTOF sensor

Highly charged solar wind ions enter the instrument (Figure 1) through the so-called wide angle variable energy (WAVE) entrance system, which has an energy-per-charge acceptance bandwidth of about half a decade and a conic field of view of $\pm 25°$ width [*Hovestadt et al.*, 1995]. The entrance system has been designed to suppress the solar wind proton flux and solar ultraviolet radiation [*Zurbuchen et al.*, 1995], both of which would saturate the instrument by start and stop counts in the isochronous spectrometer. Furthermore, WAVE reduces scattered ions and neutrals to a minimum. On the other hand, it can transmit almost the full velocity distribution of a given solar wind species to provide optimum counting statistics. After leaving the WAVE the solar wind particles can be accelerated or decelerated to the so-called VMASS, which is a V-shaped isochronous time-of-flight spectrometer. Acceleration or deceleration is chosen to optimize their detection efficiency or to prevent them from hitting the hyperbola deflection electrode of VMASS. The V-shaped and the hyperbola deflection electrode generate an electrostatic harmonic

Table 2. Results From Measurements of the Terrestrial, Solar, and Galactic Neon Isotopic Composition

$^{20}Ne/^{22}Ne$	$^{20}Ne/^{21}Ne$	Source	Reference
9.78 ± 0.03	335 ± 12	terrestrial	*Holden* [1993]
13.7 ± 0.3	420 ± 50	solar wind (Apollo foils)	*Geiss et al.* [1972]
11.2 ± 0.2	415 ± 6	SEP derived from lunar samples	*Benkert et al.* [1993]
9.2 ± 2.2	>70	SEP from flare, Sept. 23, 1978	*Mewaldt et al.* [1984]
13.2 ± 1.4	>60	SEP from flares, Oct. 30 and Nov. 2, 1992	*Selesnick et al.* [1993]
3.5 ± 1.2	>25	SEP from ^{3}He-rich flares, July 17-20, 1992	*Mason et al.* [1994]
$12.8^{+5.7}_{-6.8}$	...	anomalous cosmic rays	*Leske et al.* [1996]
2.2 ± 0.3	>20	galactic cosmic rays	*Lukasiak et al.* [1994]
13.8 ± 0.7	440 ± 110	solar wind (SOHO/CELIAS)	this work

For the solar energetic particle (SEP) isotopic abundance ratios the results for longtime averages derived from lunar samples are shown as well as the results derived from individual flare events. The solar wind results are both longtime averages.

potential so that the time of flight of an ion between start and stop detector is proportional to the square root of mass per charge $(M/Q*)^{1/2}$ and does not depend on the ion energy. The time of flight of a single ion is measured between a pulse in a microchannel plate detector (Start MCP) triggered by secondary electrons released at its passage through a thin (2.1 μg/cm^2) carbon foil as start signal and the stop pulse of a position sensing ion microchannel plate detector (IMCP). The charge state distribution Q^* of the ions leaving the foil must be well understood for quantitative measurements of isotopic and elemental abundances. Typically, particles leave the foil as neutrals that can be counted by the neutral microchannel plate detector (NMCP), or they leave it singly charged. When the ions pass the carbon foil, not only do they exchange charge with the Fermi electron sea of the solid carbon, but they also lose energy by electronic and nuclear stopping, which also causes angular straggling. Energy loss and straggling as well as angular scattering are element specific and, moreover, slightly isotope specific because the nuclear stopping is mass dependent.

Appendix B: Calibration of Instrument Functions

Essentially, three instrument functions describe the detection efficiency of the MTOF sensor:

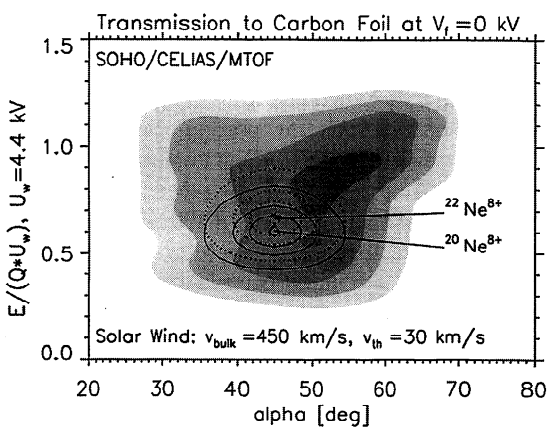

Figure B1. Acceptance function of the entrance system including the transmission to the carbon foil. This acceptance function is simply an interpolation of the actual calibration data values. The outer borders of the grey-shaded contour cells show the 20%, 40%, 60%, and 80% level in comparison with the maximum effective area of 3.2 mm^2 at a postacceleration voltage $V_f = 0$ kV. Most crucial is the dependence on energy-per-charge E/Q of the solar wind ions and on the entrance angle in the ecliptic α. In the E/Q-α plane a typical normalized solar wind distribution at the levels 0.05, 0.35, 0.65, and 0.95 is shown for the isotopes ^{20}Ne and ^{22}Ne. This distribution has to be folded with the instrument acceptance function. It is clear that this folding has a major impact on the detection efficiencies and can cause instrumental fractionation even between species such as the neon isotopes, which are separated in M/Q by 10% only.

B1. Geometry Factor

The geometry factor is determined by the ion optical transmission through the entrance system WAVE with its deflection voltage U_W onto the carbon foil, which is on a float potential V_f for postacceleration/deceleration of the solar wind ions. The ion optical acceptance of WAVE is actually the most crucial instrument characteristic to derive either elemental or isotopic abundances. As already mentioned, the energy-per-charge passband is very wide, so that a major fraction of the solar wind velocity distribution has to be folded with the instrument acceptance to determine the detection efficiency. Even for the measurement of the neon isotopic abundance ratios in a very limited mass range the WAVE acceptance plays an important role, which is visualized in Figures B1 and B2 for two different instrument settings V_f. ^{22}Ne has about the same solar wind bulk velocity and the same charge state distribution as ^{20}Ne, so that the heavier isotope has a higher center E/Q. The kinetic temperature is assumed to be proportional to the atomic mass, resulting in the same width of the drifting Maxwellian velocity distribution for both isotopes. If the E/Q solar wind distributions of the isotopes are close to a steep slope of the instrument response, the integrated efficiencies can differ by up to a factor of 2. Therefore the flight data have to be filtered with respect to instrument discrimination. The WAVE transmission to the carbon foil has been evaluated in calibrations of the integrated CELIAS flight model. Additional experiments have been performed with an identical test setup used for both the CELIAS and the ACE solar wind ion mass spectrometer (SWIMS) instruments. With these experiments it was possible to obtain additional data points in the four-dimensional parameter space established by α, β, $E/(QU_W)$, and $E/(QV_f)$, where α is the entrance angle within the ecliptic plane and β is the one perpendicular to it. Also, the effect of unwan-

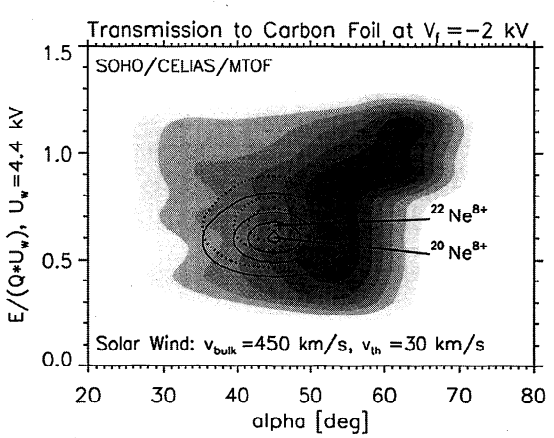

Figure B2. Same as Figure B1, but for a postacceleration voltage $V_f = -2$ kV. The contour levels are identical to Figure B1, but the effective area can be larger than 3.2 mm^2 because the negative postacceleration voltage focuses the ions onto the carbon foil of the TOF section.

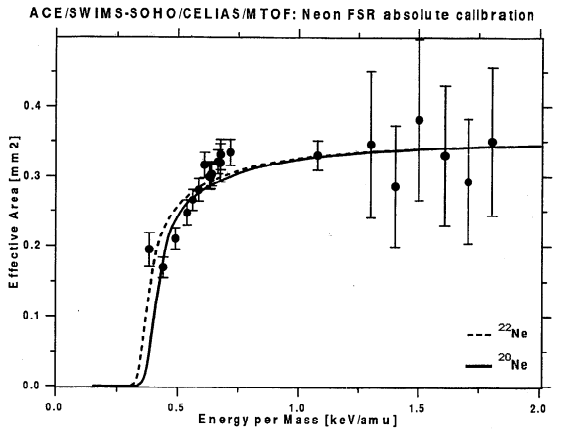

Figure B3. Front SEDA rate (FSR) calibration data and model functions versus energy per mass between 0.3 and 1.8 keV/amu. The measurements with large errors that provide the information on the saturation level of FSR have been taken with an unstable ion source but could be confirmed by calibrations with other elements. The absolute effective area of the ACE/SWIMS sensor is shown here. However, the FSR scales exactly the same way with energy per mass for CELIAS/MTOF.

ted start electrons by secondary electron emission from instrument surfaces has been investigated. The most important aim was to calibrate the focusing and defocusing effects of the V_f postacceleration voltage.

B2. Start Efficiency

The start efficiency is given by the element specific and ion velocity dependent secondary electron emission process from the carbon foil and the Start MCP efficiency. The front secondary electron detection assembly (SEDA) rate has been calibrated for many elements at typical solar wind energies in the calibration system for mass spectrometers (CASYMS) [*Steinacher et al.*, 1995] and the thermal vacuum (TV) chamber at UoB, as well as at the Strahlenzentrum of the University of Giessen [*Trassl et al.*, 1997], where not only gases but also solid elements could be used by means of an electron cyclotron resonance (ECR) ion source. The Giessen calibrations and part of the CASYMS measurements have been performed with the similar ACE SWIMS sensor. These calibrations can be well reproduced by simulations of electronic stopping in a thin carbon foil [*Ziegler et al.*, 1985]. Fitting the data leads to the conclusion that the carbon foil must be about 2.1 $\mu g/cm^2$, in accordance with the specification of the supplier, and that in a statistical sense, typically 1.5 is the minimum number of electrons that generate a start signal. Such a number has also been found for similar MCPs such as the Start MCP of ULYSSES solar wind ion composition spectrometer (SWICS). The rather small isotopic discrimination of ^{22}Ne relative to ^{20}Ne in the front SEDA rate (FSR) is illustrated in Figure B3.

B3. Double Coincidence Efficiency

The double coincidence efficiency includes the charge exchange efficiency, the energy loss and straggling in the carbon foil with the related angular scattering, the ion optical transmission of VMASS, and the IMCP stop efficiency. Experimentally determined charge state yields [*Gonin et al.*, 1994] have been used to derive the charge exchange efficiency in the carbon foil. Other data pertaining to carbon foil physics are well known from other projects such as ULYSSES SWICS or WIND MASS [*Hamilton et al.*, 1990]. On the basis of the latter the overall three-dimensional modeling of VMASS has been derived, including the position-sensing capability of the CELIAS/MTOF IMCP. To obtain the probability given by ϵ_d = DCR/FSR (double coincidence rate over FSR), all the statistical distribution functions for the energy loss and straggling, the angular straggling, and the charge exchange probability of an ion at the backside of the thin carbon foil, as well as the ion optical transmission inside VMASS, have to be taken into account. Figure B4 shows a comparison of the calibration measurements and the modeled efficiency ϵ_d of ^{20}Ne as a function of energy over mass. Figures B5 and B6 give a detailed summary of the different effects in the carbon foil and in the VMASS that cause slight isotope fractionation in ϵ_d.

Appendix C: Quantitative Evaluation of TOF spectra

One important issue in the evaluation of CELIAS/MTOF is the interference of different elements that have an approximately integer mass ratio; for example, ^{40}Ca

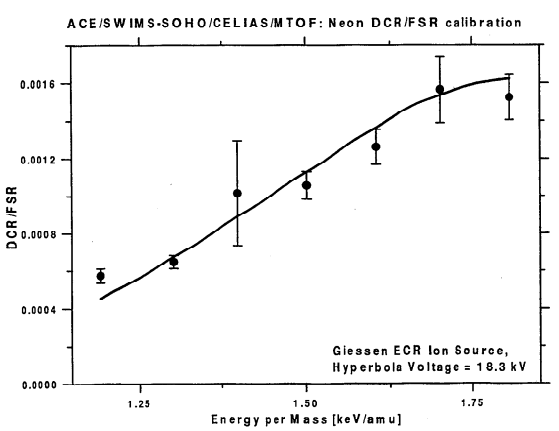

Figure B4. Double-coincidence rate DCR over FSR versus E/M for ^{20}Ne according to calibration data and a model that includes charge exchange processes, energy loss, and straggling, including its corresponding angular scattering in the carbon foil, ion optics, and stop detector efficiency. The data shown here are taken at a hyperbola electrode voltage of 18.3 kV which is close to the voltage 20.7 kV set during the mission. Only the DCR in the neon time-of-flight peak is considered; the background is subtracted. Calibrations at other hyperbola voltages have confirmed the validity of the model.

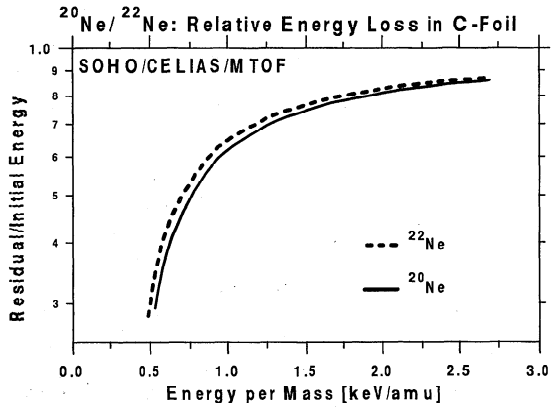

Figure B5. Relative energy loss according to simulations of electronic and nuclear stopping [*Ziegler et al.*, 1985] of the isotopes ^{20}Ne and ^{22}Ne in the thin carbon foil. At equal E/M (as in the solar wind) ^{22}Ne suffers less energy loss than ^{20}Ne and therefore has a slightly higher probability to release secondary electrons and a higher chance to be detected on the VMASS stop MCP (see Figure B6).

is twice as heavy as ^{20}Ne within 0.06%. If ^{20}Ne leaves the carbon foil singly charged and ^{40}Ca leaves doubly charged, they ideally have almost the same time of flight and cannot be resolved by the instrument. There is one reliable method to estimate the interference of doubly charged ions by calculating the instrument efficiency ratios between the ion species to be evaluated, the doubly charged interference, and its "mother peak" of singly charged ions that can be found in the same spectrum. For example, from the number of observed $^{40}Ca^{+}$ [*Gonin et al.*, 1995] we can estimate how many $^{40}Ca^{2+}$ ions will interfere with $^{20}Ne^{+}$ if the calibrated instrument functions, the instrument settings, and the solar wind parameters (bulk velocity and kinetic temperature) are known. During this work the question arose whether there are instrumental effects that shift the TOF peaks of doubly charged $^{40,42,44}Ca^{2+}$ ions against the peaks of singly charged $^{20,21,22}Ne^{+}$ ions. Both calibrations and simulations gave evidence that there is overall no larger shift than 0.3% caused by ion optical imperfections of the instrument when accumulating a typical data set over the full mission time. Therefore the doubly charged calcium interference $^{40,42,44}Ca^{2+}$ cannot be resolved in the neon spectrum of $^{20,21,22}Ne^{+}$.

Appendix D: Data Description

The following data are available:

D1. Time-of-flight Spectra

Time-of-flight spectra MT1 and MT2 are classified on board into 1024 channels and accumulated every 5 min, where MT1 and MT2 denote the IMCP position ranges farther from and closer to the carbon foil. MT1 usually has fewer counts but also much less background, so that the signal-to-noise ratio is actually better than that in MT2.

D2. Pulse Height Analysis Words

Pulse height analysis words are transferred individually for a single double-coincidence event. They contain a word (10 bits) characterizing the charge amplitude on the Start MCP, two words (10 bits each) for the stop amplitudes from the IMCP giving total charge amplitude and position, a word (12 bits) for the time of flight, and a word for the universal time of the event in seconds. Almost half the data that have been classified on board during the first 200 days of 1996 have been transferred as individual PHA words.

D3. Housekeeping Data

Housekeeping (HK) data show the regular cycling of the instrument voltages U_W and V_f (variable housekeeping) and all other commanded instrument settings or measurements at the instrument. HK values can be recorded with a time resolution of 5 min. In this work, only negative or zero postacceleration voltages V_f have been considered, because most of the neon events have

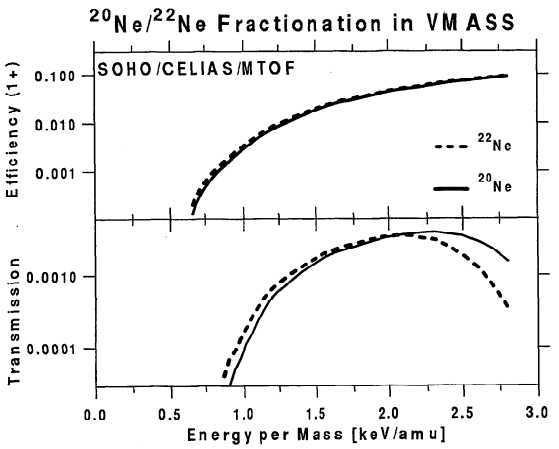

Figure B6. Probability for the isotopes ^{20}Ne and ^{22}Ne to leave the thin carbon foil singly charged versus initial energy per mass. The ionization efficiency essentially depends on the residual E/M, which is slightly higher for ^{22}Ne. Also shown is the ion optical transmission of $^{20}Ne^{+}$ and $^{22}Ne^{+}$ in VMASS. The heavier projectile $^{22}Ne^{+}$ suffers less angular scattering by nuclear stopping in the carbon foil, so that it has a higher probability to hit the stop MCP in the typical solar wind range of 0.8 to 2.0 keV/amu. Above 2.0 keV/amu, $^{22}Ne^{+}$ has a lower chance of transmission than $^{20}Ne^{+}$ because of its higher energy per charge, such that it overshoots the stop MCP or hits the hyperbola electrode. For the data evaluated in this work the isotope fractionation in VMASS is very small because only nonpositive postacceleration voltages V_f have been considered, which put the solar wind $^{20}Ne^{8+}$ onto higher initial E/M than $^{22}Ne^{8+}$ to approximately cancel the effects described above.

been collected with these settings and because the calibrations for the WAVE and the WAVE/VMASS interface are free of distortions by secondary electrons released from instrument surfaces and therefore more precise. During the mission the hyperbola deflection voltage almost exclusively was set to 20.7 kV. Only data for this setting have been selected.

D4. Proton Monitor Data

Proton monitor (PM) data for the solar wind bulk velocity v_{bulk} and its rms velocity corresponding to its kinetic temperature v_{therm} are available with a time resolution of 5 min, roughly matching the instrument cycling in the variable housekeeping data (F. M. Ipavich et al., submitted manuscript, 1997).

As we mentioned above, the TOF spectra offer a count rate about twice as high as that for the PHA data. However, as the data are classified on board, they cannot be selected for MCP signals with the lowest background, as was done with the PHA data. Therefore the absolute background remains higher by a factor of about 3.5, and the signal-to-noise ratio is correspondingly lower. ^{21}Ne can be detected in the PHA data with an uncertainty of 25% but in the MT1 spectra only with an uncertainty of more than 50%. On the other hand, the higher count rates for ^{20}Ne and ^{22}Ne in MT1 make it possible to analyze the abundance ratio ^{20}Ne/^{22}Ne as a function of the solar wind velocity and as a function of the instrument fractionation. From a time series of PHA or TOF spectra characterized by the parameters U_W, V_f, v_{bulk}, and v_{therm} the data have been selected with a detection efficiency ratio $\eta(^{22}Ne, U_W, V_f, v_{bulk}, v_{therm})$ divided by $\eta(^{20}Ne, U_W, V_f, v_{bulk}, v_{therm})$ between 0.85 and 1.15. Also, the data have been filtered for the outer stop position ranges, which gave the better signal-to-noise ratio. In addition, the TOF data have been grouped for different solar wind bulk velocities v_{bulk}.

Acknowledgments. This work was supported by the Swiss National Science Foundation, by the PRODEX program of ESA, by NASA grant NAG5-2754, and by DARA, Germany, with grants 50 OC 89056 and 50 OC 9605. The flight-spare unit of MTOF has been recalibrated with the ECR ion source of the University of Giessen and with the support of E. Salzborn and R. Trassl.

The Editor thanks Richard S. Selesnick and another referee for their assistance in evaluating this paper.

References

Anders, E., and N. Grevesse, Abundances of the elements: Meteoritic and solar, *Geochim. Cosmochim. Acta, 53*, 197–214, 1989.

Benkert, J.-P., H. Baur, P. Signer, and R. Wieler, He, Ne, and Ar from the solar wind and solar energetic particles in lunar ilmenites and pyroxenes, *J. Geophys. Res., 98*, 13,147–13,162, 1993.

Bochsler, P., H. Balsiger, R. Bodmer, O. Kern, T. Zurbuchen, G. Gloeckler, D. C. Hamilton, M. R. Collier, and D. Hovestadt, Limits to the efficiency of isotope fractionation processes in the solar wind derived from the magnesium isotopic composition as observed with the WIND/MASS experiment, *Phys. Chem. Earth*, in press, 1997.

Bochsler, P., and R. Kallenbach, Fractionation of nitrogen isotopes in solar energetic particles, *Meteoritics, 29*, 653–658, 1994.

Bodmer, R., and P. Bochsler, Fractionation of minor ions in the solar wind acceleration process, paper presented at meeting, Eur. Geophys. Soc., The Hague, Netherlands, 1996.

Geiss, J., F. Bühler, H. Cerutti, P. Eberhardt, and C. Filleux, Solar wind composition experiment, in *Apollo 16 Preliminary Scientific Report, NASA Spec. Publ., SP-315*, 14.1, 1972.

Gelb, A., J. F. Kasper, R. A. Nash, C. F. Price, and A. A. Sutherland, Optimal linear filtering, in *Applied Optimal Estimation*, edited by A. Gelb, MIT Press, Cambridge, Mass., 1974.

Gonin, M., R. Kallenbach, and P. Bochsler, Charge exchange of atoms with high first ionization potentials in carbon foils at $E \leq 35$ keV/amu, *Nucl. Instrum. Methods Phys. Res., Sect. B, 94*, 15–21, 1994.

Gonin, M., R. Kallenbach, P. Bochsler, and A. Bürgi, Charge exchange of low energy particles passing through thin carbon foils: Dependence on foil thickness and charge state yields of Mg, Ca, Ti, Cr and Ni, *Nucl. Instrum. Methods Phys. Res., Sect. B, 101*, 313–320, 1995.

Hamilton, D. C., G. Gloeckler, F. M. Ipavich, R. A. Lundgren, R. B. Sheldon, and D. Hovestadt, New high-resolution electrostatic ion mass analyzer using time of flight, *Rev. Sci. Instrum., 61*, 3104–3106, 1990.

Holden, N. E., Table of the isotopes, in *CRC Handbook of Chemistry and Physics*, edited by D. R. Lide, CRC Press, Boca Raton, Fla., 1993.

Hovestadt, D., et al., Charge, element, and isotope analysis System onboard SOHO, *Sol. Phys., 162*, 441–481, 1995.

Hunten, D. M., J.-C. Gerard, and L. M. Francois, The atmosphere's response to solar irradiation, in *The Sun in Time*, edited by C. P. Sonett, M. S. Giampapa, and M. S. Matthews, pp. 463–497, Univ. of Ariz. Press, Tucson, 1991.

Kallenbach, R., Isotope fractionation in solar energetic particles by stochastic acceleration, *ESA Spec. Publ., SP-373*, 191–194, 1994.

Leske, R. A., R. A. Mewaldt, A. C. Cummings, J. R. Cummings, E. C. Stone, and T. T. von Rosenvinge, The isotopic composition of anomalous cosmic rays from SAMPEX, *Space Sci. Rev., 78*, 149–154, 1996.

Lukasiak, A., P. Ferrando, F. B. McDonald, and W. R. Webber, Cosmic-ray isotopic composition of C, N, O, Ne, Mg, Si nuclei in the energy range 50-200 MeV per nucleon measured by the Voyager spacecraft during the solar minimum period, *Astrophys. J., 426*, 366–372, 1994.

Mason, G. M., J. E. Mazur, and D. C. Hamilton, Heavy-ion isotopic anomalies in ^{3}He-rich solar particle events, *Astrophys. J., 425*, 843–848, 1994.

Mewaldt, R. A., J. D. Spalding, and E. C. Stone, A high-resolution study of the isotopes of solar flare nuclei, *Astrophys. J., 280*, 892–901, 1984.

Selesnick, R. S., A. C. Cummings, J. R. Cummings, R. A. Leske, R. A. Mewaldt, E. C. Stone, and T. von Rosevinge, Coronal abundances of neon and magnesium isotopes from solar energetic particles, *Astrophys. J., 418*, L45–L48, 1993.

Steinacher, M., F. Jost, and U. Schwab, A modern and fully automated calibration system for space ion mass spectrometers, *Rev. Sci. Instrum., 66*, 4180–4187, 1995.

Trassl, R., P. Hathiramani, F. Broetz, J. B. Greenwood, R. W. McCullough, M. Schlapp, and E. Salzborn, Characterization and recent modifications of a compact 10

GHz electron cyclotron resonance (ECR) ion source for atomic physics experiments, *Phys. Scripta, Sect. T, 73*, 380–381, 1997.

Ziegler, J. F., J. P. Biersack, and U. Littmark, in *The stopping and range of ions in matter*, Pergamon Press, New York, 1985.

Zurbuchen, T., P. Bochsler, and F. Scholze, Reflection of ultraviolet light at 121.6 nm from rough surfaces, *Opt. Eng., 34*, 1303–1315, 1995.

W. I. Axford, H. Grünwaldt, M. Hilchenbach, S. Livi, E. Marsch, and B. Wilken, Max-Planck-Institut für Aeronomie, Max-Planck-Strasse 2, D-37189 Katlenburg-Lindau, Germany. (e-mail: gruenwaldt@linmpi.mpae.gwdg.de, hilchenbach@linax2.mpae.gwdg.de)

H. Balsiger, P. Bochsler, S. Hefti, and P. Wurz, Physikalisches Institut der Universität Bern, Sidlerstrasse 5, CH-3012 Bern, Switzerland. (e-mail: bochsler@soho.unibe.ch, hefti@soho.unibe.ch, wurz@soho.unibe.ch)

A. Bürgi, D. Hovestadt, B. Klecker, and M. Scholer, Max-Planck-Institut für Extraterrestrische Physik, Giessenbachstrasse, D-85740 Garching, Germany. (e-mail: bek@mpe.mpe-garching.mpg.de)

M. A. Coplan, A. B. Galvin, G. Gloeckler, and F. M. Ipavich, Department of Physics and Astronomy, University of Maryland, College Park, MD 20742. (e-mail: ipavich@umdsp.umd.edu)

J. Geiss and R. Kallenbach, International Space Science Institute, Hallerstrasse 6, CH-3012 Bern, Switzerland. (e-mail: geiss@issi.unibe.ch, kallenbach@soho.unibe.ch)

F. Gliem and K.-U. Reiche, Institut für Datenverarbeitungsanlagen, Technische Universität, Hans-Sommer-Strasse 66, D-38106 Braunschweig, Germany. (e-mail: gliem@ida.ing.tu-bs.de, reiche@ida.ing.tu-bs.de)

K. C. Hsieh, Department of Physics, University of Arizona, Tucson, AZ 85721.

M. A. Lee and E. Möbius, Institute for the Study of Earth, Oceans, and Space, University of New Hampshire, Morse Hall, Durham, NH 03824.

G. G. Managadze and M. I. Verigin, IKI Space Research Institute, Russian Academy of Sciences, Profsoyuznaya 84/32, 117810 Moscow, Russia.

M. Neugebauer, Jet Propulsion Laboratory, 4500 Oak Grove Drive, Pasadena, CA 91103.

(Received April 10, 1997; revised August 1, 1997;
accepted August 6, 1997.)